PHYSICAL REVIEW A **109**, 053501 (2024)

# Amplitude-modulated mirror pulses for improved cold-atom gravimetry

Yida Wang, Jinshuo Cheng, Yujuan Liu, and Tingting Lin[*]
*Key Laboratory of Geophysical Exploration Equipment, Ministry of Education, Jilin University, Changchun 130061, China and College of Instrumentation and Electrical Engineering, Jilin University, Changchun 130061, China*

(Received 5 December 2023; revised 29 March 2024; accepted 2 April 2024; published 2 May 2024)

Cold-atom gravimetry is susceptible to environmental factors and noise resulting from the expansion of the atom cloud, thereby impacting the quality of gravity signals. An amplitude-modulated mirror-pulse scheme for cold-atom gravimeters is proposed to enhance the stability of the gravity measurement. The amplitude-modulated pulse is calculated based on the combined optimal control method of differential evolution and gradient ascent pulse engineering. This combination imparts high robustness to the amplitude-modulated pulse against detuning and coupling strength. Numerical modeling of the atom gravimeter with a cloud of 3 μK $^{87}$Rb atoms suggests that, compared with the rectangular pulse, the amplitude-modulated mirror pulse reduces the uncertainty of the gravity value extracted from a single interference fringe, increases the contrast of the interference fringe by about 1.5 times, and improves the stability of the gravity measurement. Additionally, by imposing constraints on pulse-shape smoothness, the phase-noise transfer function of the gravimeter using the amplitude-modulated mirror pulse closely approximates the performance of the rectangular pulse.

DOI: 10.1103/PhysRevA.109.053501

## I. INTRODUCTION

Atom-interferometry sensors can obtain ultrahigh-precision measurements in diverse fields, including inertial measurements [1–3], the determination of fundamental constants [4,5], and tests of the weak-equivalence principle [6,7]. Cold-atom absolute gravimetry, primarily reliant on the Mach-Zehnder three-pulse atom-interferometry principle [8], provides the advantage of automatic cycle measurement without mechanical friction. It can be employed in domains such as volcano [9] and earthquake monitoring [10], oceanography [11], and resource exploration. The fidelity of the coherent manipulation of quantum states constitutes a critical factor that influences the precision of cold-atom absolute gravimetry.

The practical application of atom gravimeters necessitates dealing with adverse field conditions, including the nonuniformity of the bias magnetic field and fluctuations in the Raman laser frequency and intensity [12,13]. Moreover, during the free-fall process of the atom cloud, nonuniform longitudinal velocity distributions and horizontal expansion can occur [14,15]. Due to limitations in laser power, typical cold-atom gravimeters employ long-duration, low-intensity rectangular pulses. The pulses are sensitive to the Doppler shift and exhibit a Gaussian-shaped horizontal intensity distribution. When the laser interacts with the atom cloud, the fidelity of the quantum states manipulated by the pulse decreases. Consequently, the contrast of interference fringes is diminished, and the sensitivity of atom interferometry is limited [16].

Composite pulses [17,18] and modulated pulses [19–21] are control signals developed in the field of nuclear-magnetic-resonance spectroscopy. They are capable of robustly handling variations in coupling strength and detuning. Composite pulses comprise multiple single pulses organized in a specific sequence designed to reduce systematic errors. Although the principles of pulse manipulation for atom interferometry differ from those of nuclear magnetic resonance, several composite-pulse schemes have been applied in atom interferometry to achieve robust quantum state manipulation [22,23]. However, it is essential to consider the effects of variations in sequence length. Pulse shaping involves the modulation of the pulse amplitude or phase and has been extensively utilized in the field of quantum information processing to construct quantum gates [24,25]. Phase-modulated pulses have been shown to enhance fringe contrast in atom interferometry [26,27]. However, atom gravimeters often employ frequency chirping and are vulnerable to environmental vibrations [28,29], which can impact the interference phase. These influences can disrupt the implementation of pulse phase modulation. Therefore, it is necessary to establish robust pulses for atom gravimetry through pulse-amplitude-shaping methods, where changes in coupling strength are not intertwined with phase [30]. Compared with the rectangular $\pi$ pulse, the transition response of the rectangular $\pi/2$ pulse is superior under the same disturbance, and the quantum state after evolution is closer to the target state. Therefore, it is highly meaningful to explore the optimization of the $\pi$ pulse for Mach-Zehnder-type atom gravimeters.

In this paper, we design an amplitude-modulated mirror pulse for atom gravimeters and discuss its impact on improving gravity measurement. We employ a combination of differential evolution (DE) [31] and gradient ascent pulse engineering (GRAPE) [32], a quantum optimal control algorithm based on the limited-memory Broyden-Fletcher-Goldfarb-Shanno (L-BFGS-B) algorithm, to optimize the amplitude shape of the mirror pulse. In this scheme, we

---

[*] ttlin@jlu.edu.cn

implement a second-order finite-difference method to impose constraints on the smoothness of the mirror pulses. Additionally, we enforce boundary conditions to ensure that the amplitude range remains within the effective Rabi frequency of the rectangular mirror pulse. We examine the response of pulses optimized using state-to-state and gate-synthesis methods to detuning and coupling strength [33,34]. Utilizing a numerical simulation system for the $^{87}$Rb atom gravimeter, we investigate the impact of the amplitude-modulated mirror pulse on single interference fringes and the resultant enhancement in the stability of the gravity measurement. The sensitivity-function curve and the phase-noise transfer function of a gravimeter with an amplitude-modulated mirror pulse are solved.

## II. PULSE-SHAPING METHOD

### A. Quantum state evolution

Atom-interferometry gravimeters are typically based on two-photon stimulated Raman transition. In the process of interference of the rubidium-atom ensemble, it can be regarded as a two-level system. The quantum state in the Bloch sphere can be expressed as follows [35]:

$$|\psi\rangle = \cos\left(\frac{\nu}{2}\right)|0\rangle + e^{i\varphi}\sin\left(\frac{\nu}{2}\right)|1\rangle, \tag{1}$$

where $\nu$ and $\varphi$ are the polar and azimuth coordinates of the points on the surface of the Bloch sphere, $|0\rangle$ represents the ground state, and $|1\rangle$ represents the excited state. The Hamiltonian of its interaction with the laser can be written in the rotating coordinate system as

$$H = \frac{\hbar}{2}\mathbf{\Omega}_R \cdot \boldsymbol{\sigma}, \tag{2}$$

where $\boldsymbol{\sigma}$ is the vector of the Pauli matrix and $\mathbf{\Omega}_R$ is the field vector. It can be expressed as

$$\mathbf{\Omega}_R = \Omega_{\text{eff}}\cos(\phi_L)\boldsymbol{x} + \Omega_{\text{eff}}\cos(\phi_L)\boldsymbol{y} + \delta\boldsymbol{z}, \tag{3}$$

where $\Omega_{\text{eff}}$ is the effective Rabi frequency, $\phi_L$ is the Raman laser phase, and $\delta(t)$ is the two-photon detuning [36]:

$$\begin{aligned}\delta(t) &= \omega_1(t) - \omega_2(t)\\ &\quad - \left(\omega_{eg} + \frac{\boldsymbol{P}\cdot\boldsymbol{k}_{\text{eff}}}{m} + \frac{\hbar|\boldsymbol{k}_{\text{eff}}|^2}{2m} + \boldsymbol{k}_{\text{eff}}\cdot\boldsymbol{v}\right) + \delta^{\text{ac}}.\end{aligned} \tag{4}$$

Here $\omega_1(t)$ and $\omega_2(t)$ represent the frequencies of the two Raman laser beams, and $\omega_{eg}$ represents the energy-level difference between the ground state and the excited state. $\boldsymbol{k}_{\text{eff}}$ is the Raman wave vector $\boldsymbol{k}_1 - \boldsymbol{k}_2$. $Pk_{\text{eff}}/m$ is the Doppler shift caused by the free fall of the atom cloud, which records information about the acceleration of gravity. $\hbar|\boldsymbol{k}_{\text{eff}}|^2/2m$ is the recoil shift, $\boldsymbol{k}_{\text{eff}}\cdot v$ is the frequency shift caused by the relative speed of each atom to the center of the atom cloud, and $\delta^{\text{ac}}$ is the ac Stark shift. The interaction between the laser pulse and atoms and the two-photon Raman transition process in the Mach-Zehnder atom-interferometry gravimeter is shown in Fig. 1.

The matrix representation of the Hamiltonian is

$$H = \frac{\hbar}{2}\begin{pmatrix}\delta & \Omega_{\text{eff}}e^{-i\phi_L}\\ \Omega_{\text{eff}}e^{i\phi_L} & -\delta\end{pmatrix}. \tag{5}$$

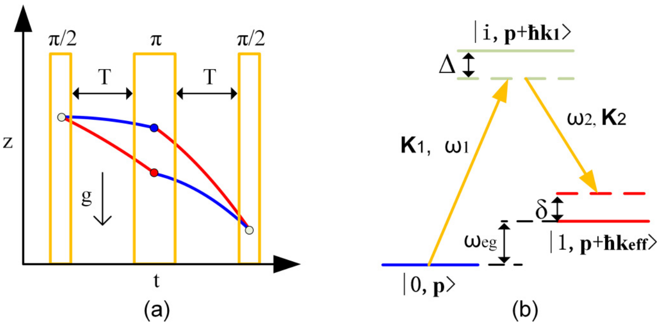

FIG. 1. (a) The interaction of laser pulses with atoms in an atom-interferometry gravimeter. (b) The two-photon Raman transition process.

The evolution of quantum states over a period of time is described by propagators [26]:

$$U = \exp\left[-i\int_0^\tau dtH(t)/\hbar\right]. \tag{6}$$

And the propagator of a Raman pulse with a duration $\Delta t$ and a constant field vector $\mathbf{\Omega}_R$ can be expressed as [22]

$$U(\theta, \phi_L, \alpha) = \begin{pmatrix}C^* & -iS^*\\ -iS & C\end{pmatrix}, \tag{7}$$

with

$$C = \cos(\Omega_R\Delta t/2) - i\sin\alpha\sin(\Omega_R\Delta t/2), \tag{8}$$

$$S = e^{i\phi_L}\cos\alpha\sin(\Omega_R\Delta t/2), \tag{9}$$

where $\alpha$ is the polar angle of the rotation axis determined by the field vector, that is, $\alpha = \arcsin(\delta/\Omega_R)$ and $\Omega_R = \sqrt{\delta^2 + \Omega_{\text{eff}}^2}$. The angle of rotation of the state vector $|\psi\rangle$ around the rotation axis of the field vector $\mathbf{\Omega}_R$ on the Bloch sphere is calculated using $\theta = \Omega_R\Delta t$. Furthermore, the quantum state $|\psi_e\rangle$ after evolution can be obtained through the propagator, which is denoted as

$$|\psi_e\rangle = U|\psi\rangle. \tag{10}$$

### B. Atom-cloud expansion and contrast loss

The horizontal intensity distribution of the Raman laser in the ideal cold-atom gravimeter is consistent, and the laser frequency remains stable. Furthermore, all atoms freely fall at the same velocity, ensuring that all atoms experience the same Raman pulse area $\Omega_R t$. In practice, due to the thermal motion of atoms, the cold-atom cloud undergoes expansion. The positions and velocity distributions of these atoms follow a Gaussian distribution and are mutually independent. The probability distribution in phase space can be expressed as follows [37]:

$$N(x, y, z, v_x, v_y, v_z) = \prod_{\mu\in\{x,y,z\}} f(\mu_0, \sigma_0)f(v_{\mu_0}, \sigma_v), \tag{11}$$

where $f$ represents a one-dimensional Gaussian distribution. The atom cloud possesses a longitudinal relative velocity distribution $f(v_{\mu_z}, \sigma_{v_z})$, which results in an overall two-photon detuning $k_{\text{eff}}f(v_{\mu_z}, \sigma_{v_z})$. For the initial state of an atom cloud in a low-energy level, when we consider only the longitudinal velocity distribution, the Raman transition probability is the integral of the atomic longitudinal velocity distribution [38]:

$$P_v = \int_{-\infty}^{\infty} f(v_{\mu_0}, \sigma_v)|S_v|^2 dv, \tag{12}$$

where $S_v$ represents the elements of the propagation operator influenced by the relative velocities of atoms. When we consider only the velocity distribution of the atom cloud and the intensity of the Raman beam, the horizontal intensity distribution of the Raman beam can be expressed as follows:

$$\Omega_{\text{eff}}(r) = \Omega_0 \exp\left[-\frac{2r^2}{w^2}\right], \tag{13}$$

where $\Omega_0$ represents the Rabi frequency at the center of the Raman beam and $w$ refers to the radius of the Raman beam. Therefore, the coupling strength experienced by atoms at different positions varies, and the Raman transition probability in cylindrical coordinates can be expressed as

$$P_\Omega = \int_{-\infty}^{\infty}\int_{0}^{\infty} N_0 \exp\left(-\frac{r^2+z^2}{2a(t)^2}\right)|S_\Omega|^2 dr dz, \tag{14}$$

where $N_0$ represents the density at the center of the atomic ensemble, $a(t)$ is the Gaussian radius of the atom cloud at time $t$, and $S_\Omega$ denotes the propagation operator elements influenced by the uneven distribution of Rabi frequencies. The propagator $U$ is altered due to the expansion of the atom cloud, resulting in a decrease in transition probability under single-pulse excitation.

For the case of a three-pulse Mach-Zehnder gravimeter with pulse interval time $T$ and chirp rate $\alpha$, the final transition probability is [39]

$$\begin{aligned} P_e = {} & |C_{\pi/2}|^4|S_\pi|^2 + 2|S_{\pi/2}|^2|C_\pi|^2|C_{\pi/2}|^2 + |S_{\pi/2}|^4|S_\pi|^2 \\ & - 2\text{Re}[e^{i\phi_g}C_{\pi/2}S_{\pi/2}(S_\pi^*)^2C_{\pi/2}^*S_{\pi/2}]. \end{aligned} \tag{15}$$

It can be converted to cosine form:

$$P_e = A(\delta) - \frac{B(\delta)}{2}\cos[\phi_g + \Phi(\delta)], \tag{16}$$

where $\phi_g$ represents the interference phase due to the gravitational effect $-k_{\text{eff}}gT^2$, $\Phi(\delta)$ denotes the phase shift introduced by the three Raman pulse phases $\phi S_{\pi/2}^1 + \phi S_{\pi/2}^3 - 2\phi S_\pi$, and it equals $\alpha T^2$ when there is no additional phase noise. $A(\delta)$ represents the bias of the interference fringe, while $B(\delta)$ denotes the contrast $4|C_{\pi/2}|^2|S_\pi|^2|S_{\pi/2}|^2$. Therefore, the longitudinal velocity distribution and horizontal expansion of the atom cloud, as well as the uneven distribution of the horizontal intensity of the Raman beam, deteriorate the propagators and cause the loss of the contrast of the interference fringe.

### C. Optimal control objective

In comparison to rectangular mirror pulses, smoother pulse shapes exhibiting amplitude-time-varying characteristics may yield superior transition and phase responses, thereby altering the robustness to detuning and coupling strength. The effective Rabi frequency governing the two-photon Raman transition is contingent upon the intensity of the dual-laser source:

$$\Omega_{\text{eff}}(t) = \frac{\Omega_e(t)^*\Omega_g(t)}{2\Delta}e^{i\phi_L} = \frac{\Gamma^2\sqrt{I_e(t)I_g(t)}}{2\Delta I_s}e^{i\phi_L}, \tag{17}$$

where $I_e(t)$ and $I_g(t)$ represent the intensities of the two Raman lasers, $\Delta$ denotes the single-photon detuning, $I_s$ and $\Gamma$ signify the saturation intensity and the natural linewidth of the atom, respectively, and $\phi_L$ stands for the phase difference between the two lasers. Two Raman beams merge and pass through an acousto-optic modulator (AOM). When the laser intensity is modulated over time, the ac Stark shift of the two ground states changes correspondingly. The differential ac Stark shift between the two states matters can be eliminated by adjusting the intensity ratio of the two lasers [38].

Quantum optimal control utilizes the concept of piecewise constants, wherein the temporal evolution of a system is discretized equidistantly into multiple segments, each of which incorporates a constant control input. The Hamiltonian is computed at each time step to determine the optimal control parameter, facilitating the attainment of optimal control. Upon segmentation of the control pulses, the propagator adopts the form of the product of $N$ segmenting operators, with each operator spanning a time step $\Delta t$:

$$U = \prod_{k}^{N} U_k = \prod_{k}^{N} \exp\left[\frac{i}{\hbar}\left(H^{(0)} + \sum_{n=1}^{2} c_k^{(n)}H^{(n)}\right)\Delta t_k\right], \tag{18}$$

where $c_k^1$ is the same as $c_k^2$, which is the effective Rabi frequency $\Omega_{\text{eff}}$. The effective Rabi frequency of the segmented pulse is optimally controlled to maximize the fidelity between the final evolved state and the target state. For $\pi$-pulse optimization, there are two methods: state to state and gate synthesis. If the optimization goal is state to state, the initial state can be set to $X_0 = |0\rangle$. For the $\pi$ pulse, the target state is $X_{\text{targ}} = |1\rangle$, and the evolved state $X_N$ is

$$X_N = U_N U_{N-1} \cdots U_2 U_1 |0\rangle. \tag{19}$$

If the goal is gate synthesis, the initial matrix can be set to the identity matrix $E$, and when $\phi_{\text{eff}}$ is zero, the target gate of the $\pi$ pulse can be set to

$$X_{\text{targ}} = \begin{bmatrix} 0 & -1j \\ -1j & 0 \end{bmatrix}. \tag{20}$$

The propagator of the finally evolved gate is

$$X_N = U_N U_{N-1} \cdots U_2 U_1 E. \tag{21}$$

The objective of optimal control is the fidelity of $X_{\text{targ}}$ and $X_N$. In the optimization process, it is necessary to try two different fidelity definitions and choose the best control scheme. When taking the real part of the inner product of two quantum states as the fidelity, the global phase should be taken into account. Conversely, when taking the modulus of the inner product of two quantum states as the fidelity, the global phase can be disregarded.

Furthermore, it is meaningful to limit the smoothness of the pulse [40]. For this purpose, the sum of the squares of the second-order differences within sequence $\Omega_{\text{eff}}(k)$ is incorporated into the fidelity as a term denoting smoothness. This addition serves as the control objective:

$$S = \lambda \sum_{k=1}^{N-3} [\Omega_{\text{eff}}(k+2) - 2\Omega_{\text{eff}}(k+1) + \Omega_{\text{eff}}(k)]^2, \quad (22)$$

where $\lambda$ is used as the smoothing coefficient to adjust the influence of the smoothing term on the overall control target. Given that the edge flatness of the pulse will impact the suppression effect of the atom interferometer on high-frequency phase noise and the maximum amplitude should not surpass the amplitude $\Omega_{\text{rec}}$ of the rectangular $\pi$ pulse corresponding to the pulse duration, a boundary constraint is imposed on the amplitude sequence:

$$|\Omega_{\text{eff}}(k)| \leqslant \Omega_{\text{rec}}, \quad (23)$$

$$\Omega_{\text{eff}}(1), \Omega_{\text{eff}}(N) \to 0. \quad (24)$$

To enhance the robustness of the pulse against detuning and coupling strength, the primary control objective should focus on achieving higher fidelity across a range of detuning and Rabi frequency-offset conditions.

### D. Combinatorial optimization

Owing to the markedly nonlinear nature of the objective function, the pulse optimization problem is plagued by local minima, rendering the search for the globally optimal solution intricate. The selection of the initial value is an important part of gradient optimization of pulses [41]. The combination of intelligent optimization and gradient optimization is a feasible method to solve this problem, which is convenient for effectively finding the optimal solution [42]. Consequently, we employ a combined optimization strategy that integrates the DE and GRAPE algorithms.

In the global-search phase, the DE algorithm is employed to explore the initial value of the pulse-amplitude sequence. The DE algorithm is rooted in population-based evolution and possesses strong global-search capabilities, typically utilized to address continuous parameter optimization problems [43,44]. The initial population of the differential evolution can be initialized with prior knowledge. An individual is represented by a set of pulse-amplitude parameters, and within the population space of a group of individuals, variation, crossover, and selection processes are executed to accomplish evolutionary objectives. During the mutation process, three individuals are chosen from the population to generate a new individual through a linear combination:

$$v_i^{(t+1)} = x_{r1}^{(t)} + F \cdot \left(x_{r2}^{(t)} - x_{r3}^{(t)}\right), \quad (25)$$

where $x_{r1}^{(t)}$, $x_{r2}^{(t)}$, and $x_{r3}^{(t)}$ represent the $i$th dimension parameters of three individuals randomly selected from the current population, $t$ denotes the iteration rounds, and $v_i^{(t+1)}$ represents the parameter values after variation. The scaling factor $F$ is a parameter ranging from 0 to 1 that regulates the influence of the parent individual in the mutation operation. During the crossover process, the mutated individual is amalgamated with the parent individual to yield the subsequent generation of individuals:

$$u_i^{(t+1)} = \begin{cases} v_i^{(t+1)}, & \text{if } \text{rand}(\cdot) \leqslant P_{\text{CR}}, \\ x_i^{(t)}, & \text{otherwise}, \end{cases} \quad (26)$$

where $u_i^{(t+1)}$ represents the parameter value after the crossover in the $i$th dimension and rand$(\cdot)$ is a random number evenly distributed within the range [0, 1]. The crossover probability $P_{\text{CR}}$ determines the extent to which the mutant and the parent are combined in the crossover operation. By comparing the objective-function values of the variant individual and the crossed individual, the superior one is selected as the next-generation individual. This process facilitates the search for the optimal solution through iterative updates. Differential evolution introduces randomness and diversity, enabling extensive exploration of the solution space while reducing the risk of getting trapped in local minima. After a specified number of iterations, a potential initial point is identified within the pulse-amplitude parameter space. This enables faster convergence to the global optimal solution during subsequent optimization.

In the gradient-descent optimization stage, the amplitude sequence obtained by the DE method is utilized as the initial value for GRAPE optimization. The GRAPE algorithm is a widely recognized gradient-based optimization method originally developed for designing NMR pulse sequences. The GRAPE scheme, utilizing the L-BFGS-B algorithm, is employed to determine the optimal solution. The L-BFGS-B algorithm, a quasi-Newton optimization approach, obviates the need for second-derivative computations of the objective function and instead iteratively constructs an approximation of the inverse Hessian matrix [45–47]. The L-BFGS-B algorithm retains only a limited set of recent iteration information and does not require storage of a complete Hessian matrix, making it particularly well suited for high-dimensional pulse optimization problems. The precise computation of the gradient of the objective function significantly expedites the convergence process of the L-BFGS-B algorithm. Initially, the derivative of the fidelity function with respect to all control parameters at each time step must be computed. In the case of pulse-amplitude optimization, the control parameter is the effective Rabi frequency. As for the objective function for gate synthesis, the initial step is as follows:

$$\frac{\partial F}{\partial c_k^{(n)}} = F\left(U_{\text{targ}}, U_N \cdots \frac{\partial U_k}{\partial \Omega_{\text{eff}}(k)} \cdots U_1 E\right). \quad (27)$$

Here the derivative calculation of the propagator for each time step can be expressed as

$$\frac{\partial U_k}{\partial \Omega_{\text{eff}}(k)} = \frac{\partial}{\partial \Omega_{\text{eff}}(k)} \exp\left(-\frac{i}{\hbar}\left\{\frac{1}{2}\delta\sigma_z + \frac{1}{2}\Omega_{\text{eff}}(k) \times [\cos(\phi_L)\sigma_x + \sin(\phi_L)\sigma_y]\right\}\Delta t\right). \quad (28)$$

The quantum state evolution and gradient are calculated by using forward propagation and back propagation, and the pulse amplitude of each segment is updated. The final gradient is the sum of the gradient of the fidelity function and the gradient of the smooth term. The GRAPE algorithm calculates the gradient based on the current pulse shape and adjusts the pulse parameters along the direction of the gradient, gradually improving the pulse shape until optimal performance is achieved. In addition, during the DE and L-BFGS-B optimization, constraints are imposed to limit the amplitude of the pulse sequence.

## III. OPTIMIZATION AND EVALUATION

The amplitude $\Omega_{\mathrm{rec}}$ of the rectangular pulse is considered to be 1, serving as the maximum amplitude constraint in the optimization process, with a duration of $\pi$. Since excessively long pulse durations introduce more adverse factors that affect pulse quality, the duration of the mirror pulse is determined under the constraint of the maximum effective Rabi frequency amplitude. For state-to-state and gate-synthesis optimizations, optimal smoothing factors are separately determined to ensure that the optimization achieves a certain degree of smoothness without overly affecting fidelity. A range of detuning and Rabi frequency are introduced into the objective function, with detuning ranging from $-0.4$ to 0.4 and effective Rabi frequency ranging from 0.9 to 1.1.

The pulse amplitude is divided into 128 constant segments at fixed time intervals. In the process of DE optimization, the design of the initial population directly affects the starting point of the algorithm and the direction of the search process. A series of pulse shapes, including rectangular, sinc, Gaussian, and others, are selected as the initial population to ensure diversity. The results of the DE algorithm after multiple iterations are used as initial values. Combined with computed precise gradient information, the GRAPE algorithm is employed for a further local search to obtain the optimal solution.

A numerical model for a cold-atom gravimeter is established to evaluate the amplitude-modulated mirror pulse. An atom cloud consisting of $5 \times 10^4$ $^{87}$Rb atoms is created in three-dimensional space, with the velocity and position of their thermal motion following a Gaussian distribution. The Raman beam is tuned to the hyperfine levels of states $|5^2S_{1/2}, F = 1\rangle$ and $|5^2S_{1/2}, F = 2\rangle$. To achieve adiabatic elimination, a large single-photon detuning is set for the intermediate state $|5^2P_{3/2}, F = 0\rangle$. The atom cloud freely falls along the direction of the Raman beam with a certain gravitational acceleration and undergoes free expansion. The horizontal intensity of the Raman beam follows a Gaussian distribution, and the laser frequency changes chirpingly during the interference process.

## IV. RESULTS AND DISCUSSION

### A. Optimization ability

The effect of the GRAPE algorithm optimization in state-to-state mode using a standard rectangular pulse as the initial value is depicted in Fig. 2(a). The result of adding the smoothing term and the fidelity corresponding to the detuning and Rabi frequency is taken as the subfunction value, and the objective-function value is the mean of a series of subfunction values. It can be observed that the initial objective-function value obtained by the rectangular pulse is 0.532. After more than 10 iterations, the objective function converges to 0.322. This demonstrates that, despite accurately solving the gradient of the objective function, the complexity of the objective function increases significantly due to the constraints imposed by the defined regularization term and the boundary conditions. Selecting a suitable initial value is a challenging task; otherwise, it can lead GRAPE to easily converge to a local minimum within the high-dimensional solution space. Under the same conditions, the iterative curve of the objective-function value in the DE-GRAPE combinatorial optimization process is shown in Fig. 2(b). As a global optimization algorithm, the DE algorithm can efficiently search the potential solution space and find an approximate optimal solution. By setting multiple different initial values of many types, the value of the objective function converges to 0.099 after a suitable number of iterations. Subsequently, the wave form obtained through DE serves as the initial value for the GRAPE algorithm, and local gradient optimization is executed to swiftly attain a more precise solution. After exceeding 10 iterations, the value of the objective function converges to 0.034, at which point the gradient of the function falls below $10^{-5}$.

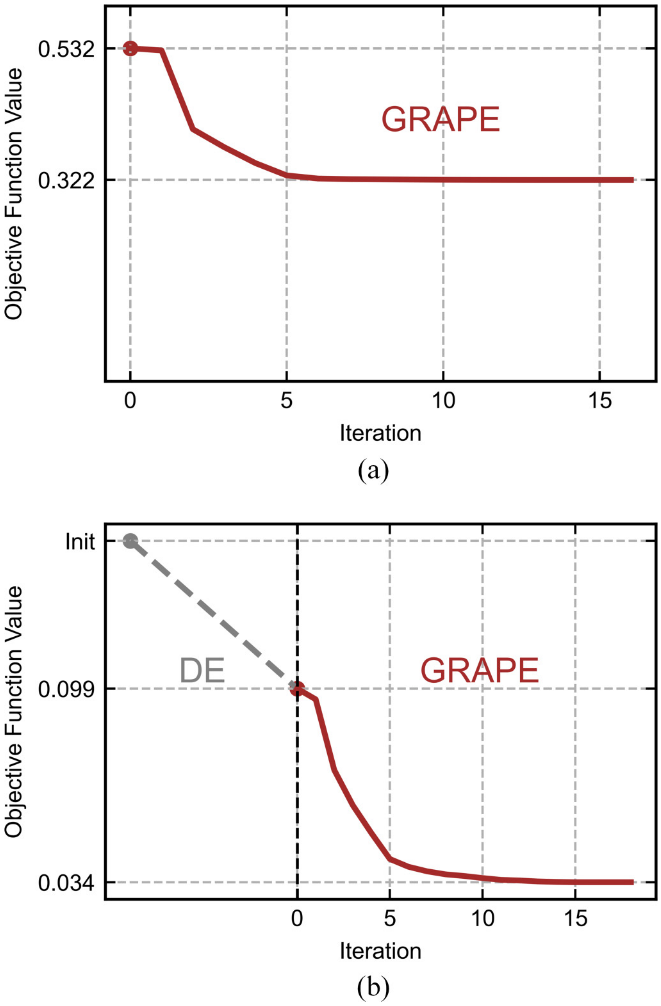

FIG. 2. (a) The iteration of the objective-function value in the GRAPE algorithm optimization process. (b) The iteration of the objective-function value in the DE-GRAPE algorithm optimization process.

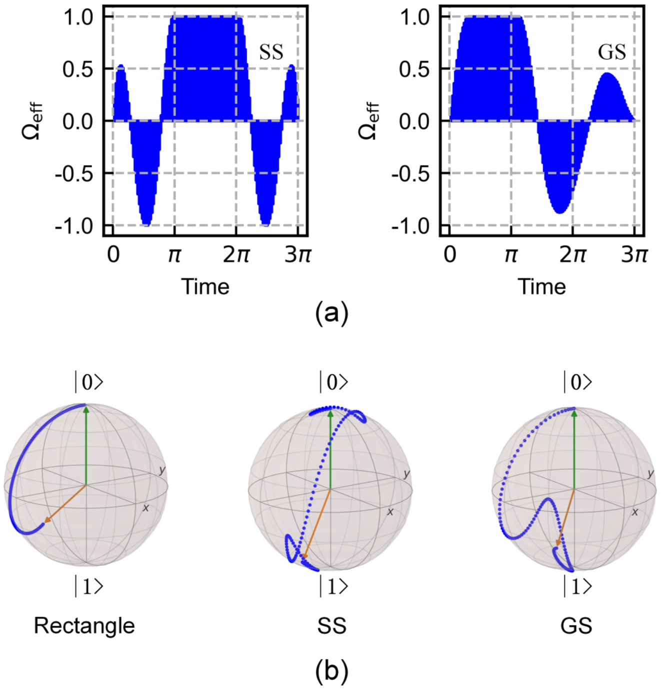

(a)

(b)

FIG. 3. (a) The shape of the pulses optimized by the state-to-state method and the gate-synthesis method. The two are denoted as the SS pulse and the GS pulse, respectively. (b) The trajectories of the quantum state evolution on the Bloch sphere start from $|0\rangle$ under the action of the rectangular, SS, and GS pulses when the Raman detuning $\delta$ is set to $+0.2\Omega_{\mathrm{rec}}$.

### B. Pulse performance

The results of pulse shaping using state-to-state and gate-synthesis methods are shown in Fig. 3(a), referred to as the SS pulse and the GS pulse, respectively. It can be seen that the SS pulse exhibits symmetry. During the optimization process, a balance between pulse duration and performance needs to be achieved, with both SS and GS pulses ultimately set to a duration of $3\pi$. Under the control of the smoothness regularization term, the optimized pulse amplitudes are sufficiently smooth to meet the hardware response capability. Two Raman beams are phase locked through an optical phase-locked loop and combined to pass through an AOM. By adjusting the power of the radio-frequency signal injected into the AOM using a wave-form generator, the intensities of the two output Raman beams can simultaneously vary to form arbitrary pulse shapes. For a negative Rabi frequency of the pulse, this can be achieved by setting the $\pi$ phase shift at the zero crossing of the amplitude. It requires a wave-form generator combined with a sufficiently fast phase jump.

For a detuning $\delta$ of $+0.2\Omega_{\mathrm{rec}}$, the evolution trajectory of quantum states on the Bloch sphere from the low-energy level $|0\rangle$ to the high-energy level $|1\rangle$ under the action of three types of mirror pulses is shown in Fig. 3(b). It is observed that under the action of the rectangular pulse, the trajectory of a quantum state rotating around the $x$ axis deviates significantly. In contrast, the evolution trajectories under the SS- and GS-pulse actions are more complex, and their final states are closer to the high-energy level. Level transitions exhibit a certain degree of robustness against detuning.

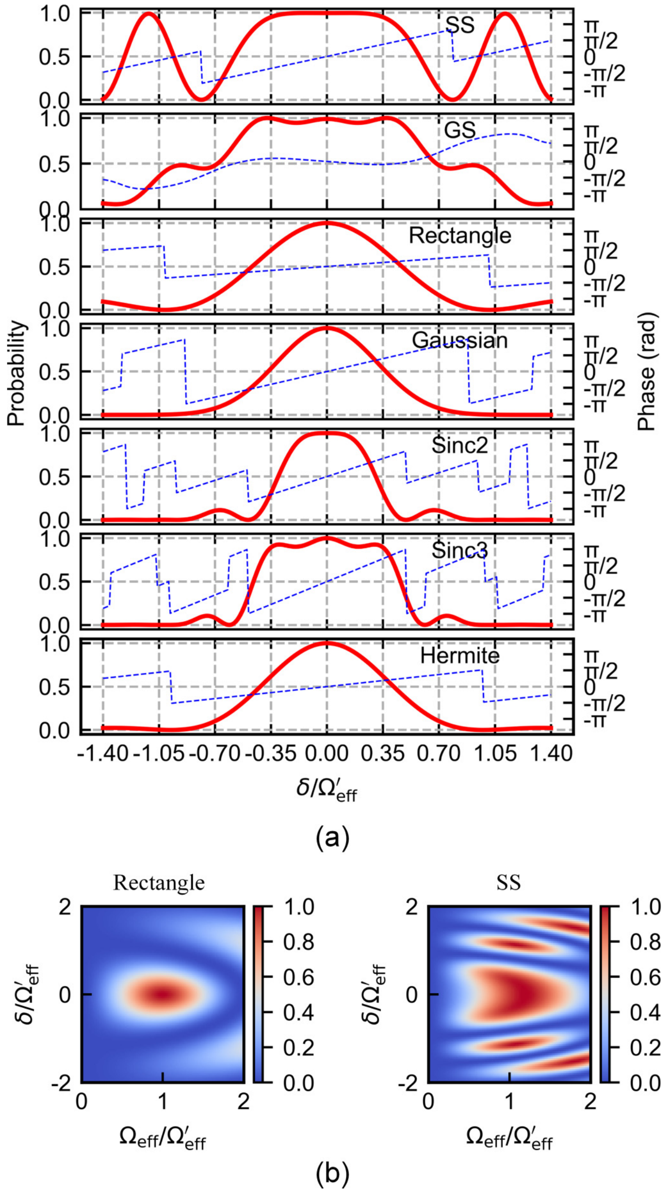

(a)

(b)

FIG. 4. (a) Transition-probability response (red solid line) and phase response (blue dashed line) of various amplitude-modulated mirror pulses to detuning. (b) The transition-probability response of the rectangular pulse and the SS pulse to detuning and coupling strength.

The transition probability response of some typical amplitude-modulated mirror pulses to detuning and the phase response of the propagator element S are shown in Fig. 4(a), where $\Omega'_{\mathrm{eff}}$ is $2\pi \times 25$ kHz. The response to detuning reflects the robustness of the pulses against Doppler shifts, Zeeman frequency shifts, and laser frequency fluctuation. The standard deviation of the Gaussian pulse is set to 0.4, and it is truncated at 4 times the standard deviation. The sinc2 and sinc3 pulses are truncated versions of the sinc wave form at the second and third zero crossings, respectively. A Hermite pulse is generated by specifying control points, tangent vectors, and four basis functions. The peak amplitudes of all pulses are constrained to match that of the rectangular pulse. The pulse duration is adjusted to achieve a $\pi$-pulse effect, and the time

TABLE I. Comparison of the properties of various amplitude-modulated pulses. Bandwidth refers to the range of detuning at which the transition probability is reduced to 90% or 50%.

| | | Bandwidth | |
|---|---|---|---|
| Pulse | Pulse width $\pi$ | 90% | 50% |
| SS | 3 | 0.806 | 1.16 |
| GS | 3 | 0.986 | 1.369 |
| Rectangle | 1 | 0.368 | 0.944 |
| Gaussian | 3.2 | 0.288 | 0.725 |
| Sinc2 | 4.5 | 0.369 | 0.608 |
| Sinc3 | 5.7 | 0.686 | 0.923 |
| Hermite | 1.5 | 0.337 | 0.844 |

step for each pulse is optimized to be as close as possible. It can be observed that the transition bandwidth for the SS and GS pulses is superior to that of other classical pulses. Table I shows the duration of each pulse and the bandwidth when the transition probability decreases to 90% and 50%. The phase response of the GS pulse reverses with the change in detuning in the passband region. The nonlinear phase response will ultimately affect the output phase of the interferometer, and this is related to the ability to optimize control objectives for phase control. The performance of the SS pulse and the rectangular pulse under the combined action of Rabi frequency and detuning is shown in Fig. 4(b). It can be observed that the transition effect under the action of the SS pulse is significantly superior to that of the rectangular pulse.

### C. Atom-interferometry gravity measurement

The SS pulse is tested based on the numerical model of the cold-atom-interferometry gravimeter. The local gravitational acceleration is set to 9.80664999 $\mathrm{m/s^2}$. The first and third Raman pulses are rectangular pulses with a Rabi frequency $\Omega'_{\mathrm{eff}}$ of $2\pi \times 25$ kHz. The mirror pulse is configured as the SS pulse or the rectangular pulse. The radius of the Raman laser is 10 mm. The single-photon detuning is 1.5 GHz. The triggering time of the first Raman pulse is set to 30 ms after the release of the atoms. The initial cold-atom cloud has a Gaussian radius of 1.5 mm, with an atom-cloud temperature of 3 μK, and no velocity selection is performed. The numerical model considers only the influence of detuning and the Rabi frequency. The detuning fluctuation is caused by the Gaussian longitudinal velocity distribution of the atom cloud. The Gaussian position distribution and expansion of the atom cloud, along with the Gaussian distribution of Raman light intensity, contribute to the Rabi frequency fluctuation. Only interference fringes with positive chirp rates are measured to extract gravity values. Interference fringes are obtained by scanning the chirp rate of the laser frequency and calculating the population of the final excited state of the atomic ensemble. Interference fringes resulting from the rectangular mirror pulse and the SS mirror pulse under different Raman time intervals $T$ are shown in Fig. 5(a). The reference chirp rate is $k_{\mathrm{eff}}g$ in the fitting process. The contrast and phase uncertainty of fringe fitting in various cases are given in Table II. It can be observed that the contrast of the interference fringes of the gravimeter can be enhanced by approximately 1.5 times when employing the SS mirror pulse at different Raman intervals. The SS pulse significantly diminishes the phase uncertainty of fitted fringes and the uncertainty of gravity corresponding to a single fringe.

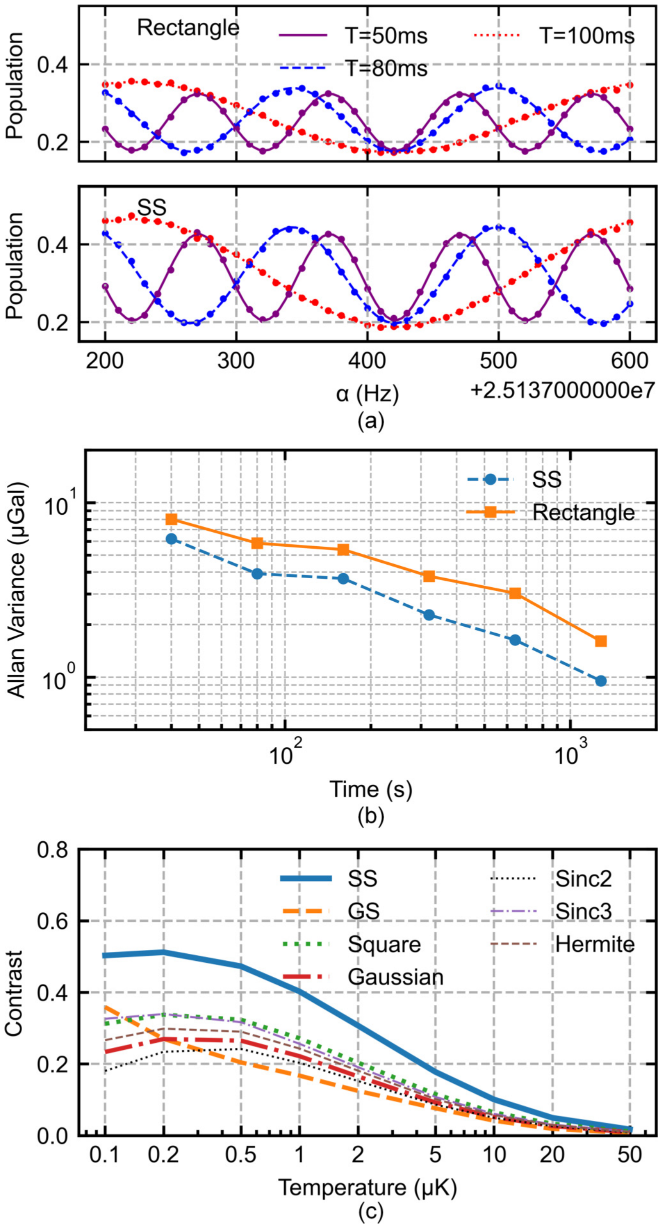

FIG. 5. (a) Interference fringes of the cold-atom gravimeter with the rectangular pulse and the SS pulse as the mirror pulses at different Raman intervals. (b) Allan variance of the gravity measurement with the cold-atom gravimeter with the rectangular pulse and the SS pulse as mirror pulses. (c) Variation of the contrast of the interference fringes of the cold-atom gravimeter with different mirror pulses as a function of the temperature of the atom cloud.

A single gravity-measurement period is set at 40 s, and 200 gravity measurements are conducted using the two pulse sequences separately through the numerical model. The Allan variance of the residual gravity measured by the two pulse schemes is calculated. The Allan variance can be employed to

TABLE II. The fitting effect of the interference fringes of the atom gravimeter with the SS pulse and the rectangular pulse as mirror pulses and the uncertainty of the phase and gravity values corresponding to a single fringe.

| $T$ (ms) | Mirror pulse | Contrast | $\pm\Phi$(mrad) | $\pm$g ($\mu$Gal) |
|---|---|---|---|---|
| 50 | Rectangle | 0.181 | 8.217 | 20.394 |
| | SS | 0.277 | 6.712 | 16.658 |
| 80 | Rectangle | 0.163 | 8.285 | 8.034 |
| | SS | 0.246 | 6.641 | 6.441 |
| 100 | Rectangle | 0.141 | 7.753 | 4.812 |
| | SS | 0.222 | 6.251 | 3.88 |

analyze and evaluate the stability of atom gravimeters. The Allan variance results for gravity measurements are shown in Fig. 5(b). It can be observed that the long-term stability of gravity measurements using the rectangular pulse and the SS pulse is 1.606 and 0.951 μGal, respectively. The SS pulse scheme is employed as the mirror pulse to enhance the stability of the gravity measurement.

For a temperature of the cold-atom cloud in the range of 0.1 to 50 μK, the change in fringe contrast of the atom gravimeter under various amplitude-modulated mirror pulses is illustrated in Fig. 5(c). The fringe contrast under the influence of classical amplitude-modulated pulses closely resembles that of the rectangular pulse. The contrast of the sinc3 pulse is slightly superior to that of the rectangular pulse at lower atom-cloud temperatures. The GS pulse exhibits a notably poor fringe contrast, primarily attributed to its reversed phase response. In contrast, the fringe contrast of the SS pulse remains significantly higher than those of other pulse types across the entire temperature range.

### D. Sensitivity function

The sensitivity function was originally used to study the degradation of atomic clocks due to the phase noise of the local oscillator. The sensitivity function of a cold-atom gravimeter can be used to describe the response of the phase of the interference fringe $\delta\Phi$ to the instantaneous change in the relative phase $\delta\phi(t)$ between two Raman lasers at a given time $t$ [48]. The sensitivity function is defined as

$$g(t) = \lim_{\delta\phi\to 0} \frac{\delta\Phi(\delta\phi, t)}{\delta\phi(t)}. \tag{29}$$

The effect of phase jumps during and between three Raman pulses on the phase of the gravimeter fringe can be quantified by the sensitivity function. This quantification enables compensation for the vibration noise and phase noise of the Raman laser. In a Mach-Zehnder sequence in which all three pulses are rectangular, the second pulse is centered at $t = 0$. The function $g(t)$ is an odd function, and for $t > 0$, the sensitivity function is as follows:

$$g(t) = \begin{cases} \sin(\Omega_r t), & 0 < t < \tau, \\ 1, & \tau < t < T + \tau, \\ -\sin[\Omega_r(T - t)], & T + \tau < t < T + 2\tau, \\ 0, & t > 2\tau, \end{cases} \tag{30}$$

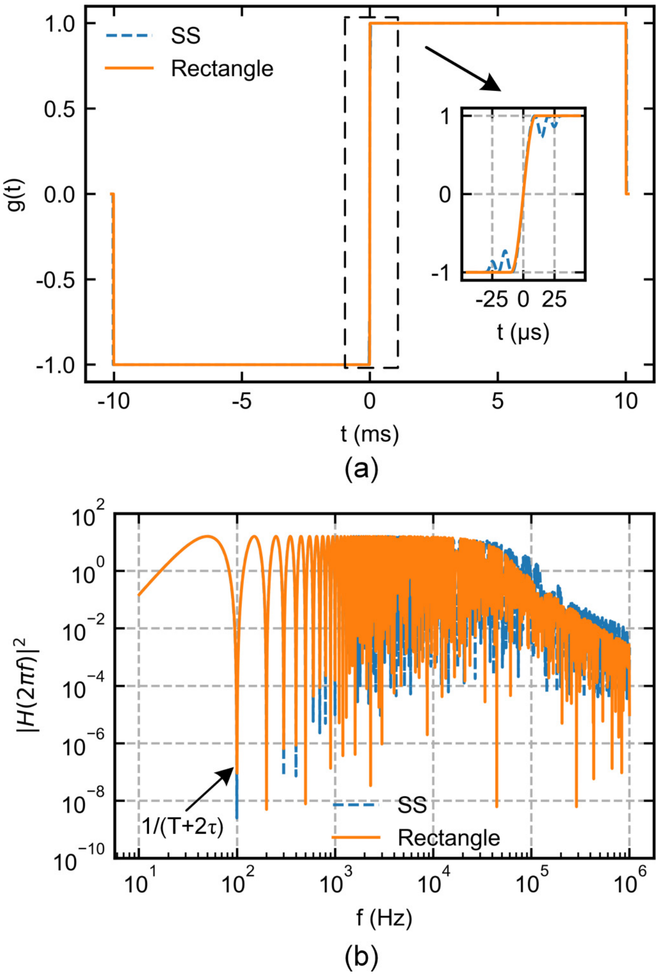

FIG. 6. (a) The sensitivity-function curves of the cold-atom gravimeter with the rectangular pulse and the SS pulse as mirror pulses. (b) The transfer functions of the cold-atom gravimeter with the rectangular pulse and the SS pulse as mirror pulses.

where $\tau$ is the length of the first and third pulses. The sensitivity-function curve of the atom gravimeter, for which the first and third pulses are rectangular and the mirror pulse is the SS pulse and the rectangular pulse, respectively, is shown in Fig. 6(a). The Raman pulse interval $T$ is 10 ms, and the peak Rabi frequency of the pulse is $2\pi \times 25$ kHz. It can be seen that for the sequence of the SS pulse as the mirror pulse, the sensitivity-function curve changes gently in the part of the mirror pulse, and the rising slope near the center is close to that of the rectangular pulse.

The change in pulse-smoothing intensity is related to the effect of the atom interferometer on suppressing high-frequency phase noise [49]. The transfer-function curves corresponding to the two sequences are shown in Fig. 6(b). For the rectangular pulse, the computation is carried out analytically, while for the SS pulse, a numerical method is employed. The transfer function of the sequence with the SS pulse as the mirror pulse in the low-frequency region is consistent with that of the rectangular pulse, and its suppression effect on the high-frequency phase noise is very close to that of the rectangular pulse. While the SS pulse exhibits a wider range of amplitude variation in the Rabi frequency, constraints are imposed on the start and end points of the pulse to limit its extent, as well as its smoothness during the pulse optimization process, to ensure that it does not deteriorate the suppression of high-frequency phase noise. This indicates that the SS pulse is also applicable for the practical implementation of atom gravimeters in real-world environments from the perspective of phase noise.

## V. CONCLUSION

In summary, an amplitude-modulated mirror-pulse scheme for atom gravimeters was designed in this study. The numerical results demonstrate that the SS mirror pulse can enhance the fitting effect of interference fringes and improve the stability of gravity measurement. In future work, we will investigate the joint optimization of the phase and amplitude of pulses in the atom gravimeter, including the design of $\pi/2$ pulses.

## ACKNOWLEDGMENTS

This work was supported in part by the National Natural Science Foundation of China under Grants No. 42330803 and No. U21A2020, in part by the National Key Research and Development Program of China under Grant No. 2022YFC3003200, and in part by the Natural Science Foundation of Jilin Province under Grant No. 20220201059GX.

[1] B. Stray *et al.*, Nature (London) **602**, 590 (2022).

[2] M. J. Snadden, J. M. McGuirk, P. Bouyer, K. G. Haritos, and M. A. Kasevich, Phys. Rev. Lett. **81**, 971 (1998).

[3] G. Biedermann, X. Wu, L. Deslauriers, S. Roy, C. Mahadeswaraswamy, and M. Kasevich, Phys. Rev. A **91**, 033629 (2015).

[4] G. Rosi, F. Sorrentino, L. Cacciapuoti, M. Prevedelli, and G. Tino, Nature (London) **510**, 518 (2014).

[5] G. Lamporesi, A. Bertoldi, L. Cacciapuoti, M. Prevedelli, and G. M. Tino, Phys. Rev. Lett. **100**, 050801 (2008).

[6] P. Asenbaum, C. Overstreet, M. Kim, J. Curti, and M. A. Kasevich, Phys. Rev. Lett. **125**, 191101 (2020).

[7] A. Bonnin, N. Zahzam, Y. Bidel, and A. Bresson, Phys. Rev. A **92**, 023626 (2015).

[8] M. Kasevich and S. Chu, Phys. Rev. Lett. **67**, 181 (1991).

[9] D. Carbone, L. Zuccarello, A. Messina, S. Scollo, and H. Rymer, Sci. Rep. **5**, 18049 (2015).

[10] J.-P. Montagner, K. Juhel, M. Barsuglia, J. P. Ampuero, E. Chassande-Mottin, J. Harms, B. Whiting, P. Bernard, E. Clévédé, and P. Lognonné, Nat. Commun. **7**, 13349 (2016).

[11] Y. Bidel, N. Zahzam, C. Blanchard, A. Bonnin, M. Cadoret, A. Bresson, D. Rouxel, and M. Lequentrec-Lalancette, Nat. Commun. **9**, 627 (2018).

[12] X. Wu, Z. Pagel, B. S. Malek, T. H. Nguyen, F. Zi, D. S. Scheirer, and H. Müller, Sci. Adv. **5**, eaax0800 (2019).

[13] Y. Bidel, O. Carraz, R. Charrière, M. Cadoret, N. Zahzam, and A. Bresson, Appl. Phys. Lett. **102**, 144107 (2013).

[14] S. W. Chiow, T. Kovachy, H.-C. Chien, and M. A. Kasevich, Phys. Rev. Lett. **107**, 130403 (2011).

[15] Q.-Q. Hu, Y.-K. Luo, A.-A. Jia, C.-H. Wei, S.-H. Yan, and J. Yang, Opt. Commun. **390**, 111 (2017).

[16] S. S. Szigeti, J. E. Debs, J. J. Hope, N. P. Robins, and J. D. Close, New J. Phys. **14**, 023009 (2012).

[17] S. Van Frank, A. Negretti, T. Berrada, R. Bücker, S. Montangero, J.-F. Schaff, T. Schumm, T. Calarco, and J. Schmiedmayer, Nat. Commun. **5**, 4009 (2014).

[18] G. Jäger, D. M. Reich, M. H. Goerz, C. P. Koch, and U. Hohenester, Phys. Rev. A **90**, 033628 (2014).

[19] D. Daems, A. Ruschhaupt, D. Sugny, and S. Guerin, Phys. Rev. Lett. **111**, 050404 (2013).

[20] P. B. Wigley *et al.*, Sci. Rep. **6**, 25890 (2016).

[21] R. Freeman, Prog. Nucl. Magn. Reson. Spectrosc. **32**, 59 (1998).

[22] A. Dunning, R. Gregory, J. Bateman, N. Cooper, M. Himsworth, J. A. Jones, and T. Freegarde, Phys. Rev. A **90**, 033608 (2014).

[23] P. Berg, S. Abend, G. Tackmann, C. Schubert, E. Giese, W. P. Schleich, F. A. Narducci, W. Ertmer, and E. M. Rasel, Phys. Rev. Lett. **114**, 063002 (2015).

[24] J. P. S. Peterson, R. S. Sarthour, and R. Laflamme, Phys. Rev. Appl. **13**, 054060 (2020).

[25] A. W. Cross and J. M. Gambetta, Phys. Rev. A **91**, 032325 (2015).

[26] J. C. Saywell, I. Kuprov, D. Goodwin, M. Carey, and T. Freegarde, Phys. Rev. A **98**, 023625 (2018).

[27] J. C. Saywell, M. Carey, M. Belal, I. Kuprov, and T. Freegarde, J. Phys. B **53**, 085006 (2020).

[28] B. Cheng, P. Gillot, S. Merlet, and F. Pereira Dos Santos, Phys. Rev. A **92**, 063617 (2015).

[29] S. Abend *et al.*, Phys. Rev. Lett. **117**, 203003 (2016).

[30] N. Dedes, J. C. Saywell, M. Carey, I. Kuprov, and T. Freegarde, Phys. Rev. A **108**, 053319 (2023).

[31] N. B. Lovett, C. Crosnier, M. Perarnau-Llobet, and B. C. Sanders, Phys. Rev. Lett. **110**, 220501 (2013).

[32] N. Khaneja, T. Reiss, C. Kehlet, T. Schulte-Herbrüggen, and S. J. Glaser, J. Magn. Reson. **172**, 296 (2005).

[33] E. T. Campbell and M. Howard, Phys. Rev. A **95**, 022316 (2017).

[34] S. Machnes, U. Sander, S. J. Glaser, P. de Fouquieres, A. Gruslys, S. Schirmer, and T. Schulte-Herbrüggen, Phys. Rev. A **84**, 022305 (2011).

[35] B. W. Shore, *Manipulating Quantum Structures Using Laser Pulses* (Cambridge University Press, Cambridge, 2011).

[36] P. R. Berman, *Atom Interferometry* (Academic, Cambridge, Massachusetts, 1997).

[37] T. M. Brzozowski, M. Maczynska, M. Zawada, J. Zachorowski, and W. Gawlik, J. Opt. B **4**, 62 (2002).

[38] Y. Luo, S. Yan, Q. Hu, A. Jia, C. Wei, and J. Yang, Eur. Phys. J. D **70**, 262 (2016).

[39] R. Stoner, D. Butts, J. Kinast, and B. Timmons, J. Opt. Soc. Am. B **28**, 2418 (2011).

[40] M. A. Janich, M. A. McLean, R. Noeske, S. J. Glaser, and R. F. Schulte, J. Magn. Reson. **223**, 129 (2012).

[41] A. R. Altenhof, A. W. Lindquist, L. D. Foster, S. T. Holmes, and R. W. Schurko, J. Magn. Reson. **309**, 106612 (2019).

[42] R. Porotti, V. Peano, and F. Marquardt, PRX Quantum **4**, 030305 (2023).

[43] N. S. Nichols, P. Sokol, and A. Del Maestro, Phys. Rev. E **106**, 025312 (2022).

[44] X. Yang, J. Li, and X. Peng, Sci. Bull. **64**, 1402 (2019).

[45] D. L. Goodwin and I. Kuprov, J. Chem. Phys. **144**, 204107 (2016).

[46] D. L. Goodwin and I. Kuprov, J. Chem. Phys. **143**, 084113 (2015).

[47] F. F. Floether, P. De Fouquieres, and S. G. Schirmer, New J. Phys. **14**, 073023 (2012).

[48] P. Cheinet, B. Canuel, F. P. Dos Santos, A. Gauguet, F. Yver-Leduc, and A. Landragin, IEEE Trans. Instrum. Meas. **57**, 1141 (2008).

[49] B. Fang, N. Mielec, D. Savoie, M. Altorio, A. Landragin, and R. Geiger, New J. Phys. **20**, 023020 (2018).